Evaluation of XRI-UNO CdTe detector for nuclear medical imaging

2015 JINST 10 P06012

(http://iopscience.iop.org/1748-0221/10/06/P06012)

PUBLISHED BY IOP PUBLISHING FOR SISSA MEDIALAB

RECEIVED: *May 1, 2015*
ACCEPTED: *May 27, 2015*
PUBLISHED: *June 22, 2015*

Evaluation of XRI-UNO CdTe detector for nuclear medical imaging

L.K. Jambi[a,b,1] **J.E. Lees,**[a] **S.L. Bugby,**[a] **S. Tipper,**[c] **M.S. Alqahtani**[a,d] **and A.C. Perkins**[e]

[a] *Space Research Centre, Department of Physics & Astronomy, University of Leicester, Leicester, LE1 7RH, U.K.*
[b] *Department of Radiological Sciences, College of Applied Medical Sciences, King Saud University, Riyadh, Kingdom of Saudi Arabia*
[c] *Department of Physics, University of Liverpool, Liverpool, L69 3BX, U.K.*
[d] *Department of Radiological Sciences, College of Applied Medical Sciences, King Khalid University, Abha, Kingdom of Saudi Arabia*
[e] *Radiological Sciences, School of Medicine, University of Nottingham, Nottingham, NG7 2UH, U.K.*

E-mail: Lj97@leicester.ac.uk

ABSTRACT: Over the last two decades advances in semiconductor detector technology have reached the point where they are sufficiently sensitive to become an alternative to scintillators for high energy gamma ray detection for application in fields such as medical imaging. This paper assessed the Cadmium-Telluride (CdTe) XRI-UNO semiconductor detector produced by X-RAY Imatek for photon energies of interest in nuclear imaging. The XRI-UNO detector was found to have an intrinsic spatial resolution of <0.5mm and a high incident count rate capability up to at least 1680cps. The system spatial resolution, uniformity and sensitivity characteristics are also reported.

KEYWORDS: Gamma detectors (scintillators, CZT, HPG, HgI etc); X-ray detectors; Image processing

[1] Corresponding author.

doi:10.1088/1748-0221/10/06/P06012

Contents

1 Introduction

In the field of medical imaging, small field of view (SFOV) gamma cameras have been developed to give high photon detection efficiency together with high spatial resolution. SFOV cameras have the potential to be used as dedicated small-organ imaging systems, such as for cardiac and breast imaging, intraoperative sentinel lymph node mapping, thyroid or parathyroid imaging and for radiopharmaceutical guided surgery [1]. Scintillation detectors and semiconductor detectors are the most commonly used radiation detectors in nuclear measurement systems to convert radiation energy into an electronic signal.

Although the use of CdTe detectors in medical imaging systems has been limited, there have been some applications of these detectors in diagnostic X-ray mammography and (SFOV) gamma imaging [2, 3]. These CdTe devices have pixel detector arrays to convert the incident photons directly into charge signals therefore offering new potential as imaging systems [4].

A fundamental phase in the management of patients with breast tumours is the assessment of the sentinel lymph nodes (SLNs) to determine if there has been tumour spread form the primary site. During breast cancer surgery the sentinel lymph nodes (SLNs) are identified using lymphoscintigraphy. The preferred radiopharmaceutical for this procedure is ^{99m}Tc labelled nanocolloid. During the operation a gamma probe is used for measuring the radioactive uptake in SLNs, however the introduction of imaging probes based on semiconductor detectors has been developed [5].

2015 JINST 10 P06012

Examples of CdTe semiconductor detection for X-ray and gamma-ray imaging indicate that the newly developed semiconductor detectors have the potential to be competitive with the existing imaging devices based on scintillators [4, 5].

We present an evaluation of the XRI-UNO CdTe-based detector for medical imaging with ^{99m}Tc and other radioactive sources [6]. The measured performance characteristics include: spatial resolution (both intrinsic and system), intrinsic spatial uniformity (integral and differential), intrinsic sensitivity, count rate capability and contrast to noise ratio.

2 Materials and methods

2.1 Properties of CdTe

Cadmium Telluride (CdTe) is an example of a semiconductor that can be used for high energy photon detection due to its high absorption properties.

The absorption of photons by a material can be calculated by:

$$I_{\text{abs}} = I_0[1 - \mathrm{e}^{-\mu t}] \tag{2.1}$$

where, I_0 is the initial intensity of photon flux, t the thickness of the attenuator and μ the linear attenuation coefficient [7].

As the photon interaction mechanisms are energy dependent, therefore the linear attenuation coefficient depends mainly on energy. The attenuation is usually expressed using the mass attenuation coefficient μ/ρ where ρ is the density of the medium (gcm^{-3}) [8]. For CdTe the mass attenuation coefficient is $0.6071\,\mathrm{cm}^2\mathrm{g}^{-1}$ at a photon energy of 150 keV and its density is $6.20\,\mathrm{gcm}^{-3}$, therefore the linear attenuation coefficient μ is $3.67\,\mathrm{cm}^{-1}$ at 150 keV.

The absorption curves for a range of CdTe thicknesses of 600, 1200 and 1400 μm are shown in figure 1 as a function of the photon energy (keV). The mass attenuation coefficients μ/ρ have been derived from the NIST database [9].

2.2 XRI-UNO system

The XRI-UNO system is an imaging device which uses the Medipix2 chip. The Medipix2 chip is a high spatial resolution, high contrast, complementary metal-oxide semiconductor (CMOS) pixel readout chip. It can be combined with different semiconductor sensors which convert the X-ray directly into detectable electric signals. The Medipix2 readout chip is bump bonded to the 1 mm thick CdTe detector. The Medipix2 measures 16.12 mm $\times$ 14.11 mm with an active area of 19.82 mm^2. It consists of 256×256 identical elements, each working in single photon counting mode for positive or negative input charge signals, each pixel occupies a total area of $55\,\mu\mathrm{m} \times 55\,\mu\mathrm{m}$. This detector normally operates at a temperature above 32° [6]. Figure 2 (top) shows a photograph of the detector with a white square indicating the active area. A schematic is also shown in figure 2 (bottom), which details the layout of the CdTe sensor within the detector casing.

Table 1 shows the physical specifications of the detector as provided by the manufacturer.

2015 JINST 10 P06012

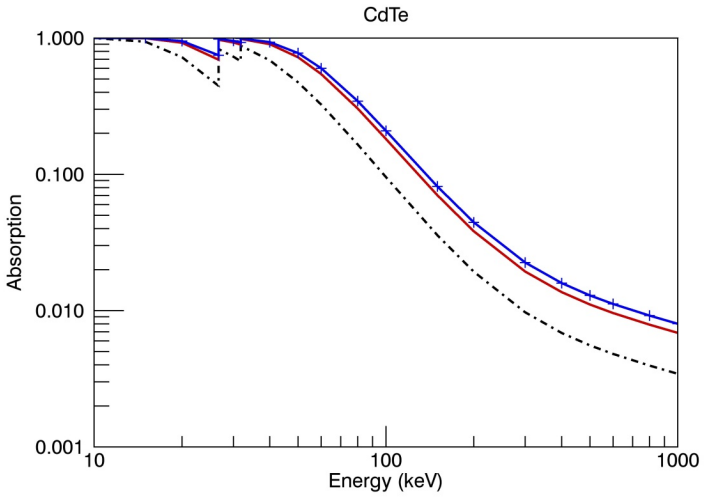

Figure 1. CdTe absorption curves for differing CdTe thickness; 600 μm (black dash-dotted line), 1200 μm (red line) and 1400 μm (blue line with plus sign).

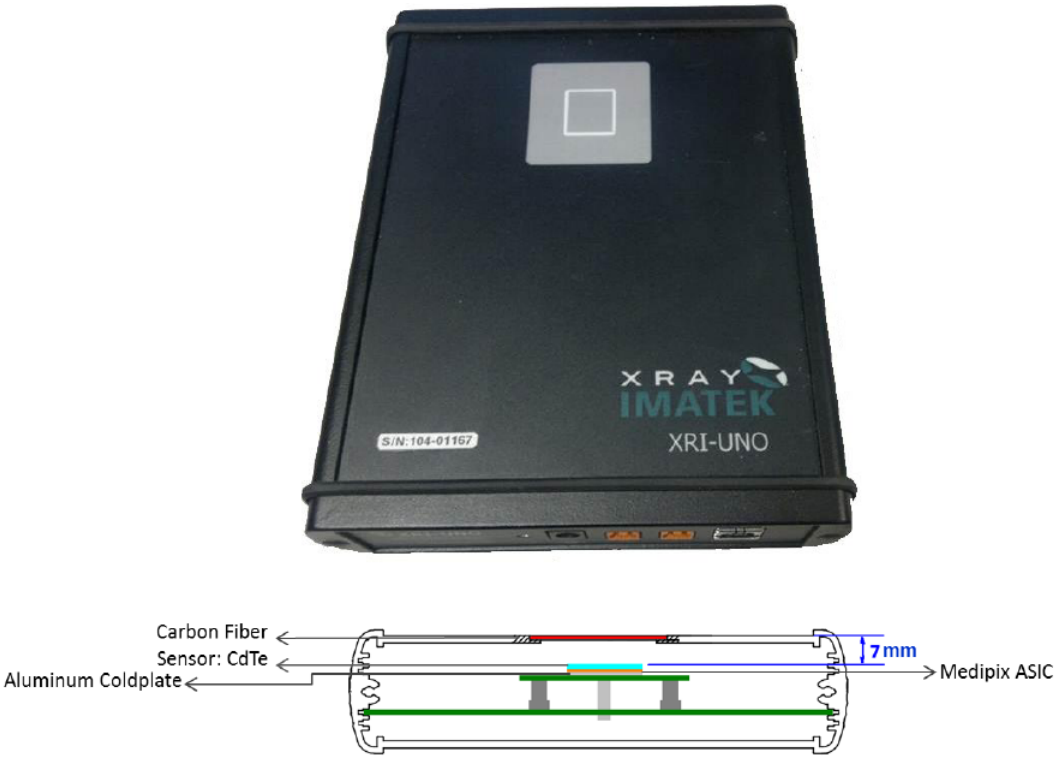

Figure 2. (Top) Image of XRI-UNO CdTe detector. The active area is the small white square in the upper part of the detector. (Bottom) Schematic of the XRI-UNO.

2015 JINST 10 P06012

Table 1. The physical specifications of the XRI-UNO CdTe detector [6].

Physical Specification	
Dimension (W $\times$ L $\times$ H)	138 mm $\times$ 172 mm $\times$ 34 mm
Weight	$\sim$ 500g
Pixel size / # Pixels	55 μm $\times$ 55 μm/65,536 pixels
Material	Cadmium Telluride
Thickness of CdTe detector	1 mm thick
Active Area	14.08 mm $\times$ 14.08 mm
Power Consumption	5W
Bias Voltage	Down to – 500V
Read-out Circuit	Bump-bonded CMOS
Hybrid Fill Factor	100 %

2.3 Imaging procedure

All images, unless otherwise specified, were subject to the same image processing; a hot pixel mask was created by taking several background images and then the internal masking program was used to mask hot pixels. Background images were taken each day and subtracted from each image. Masks were re-created about every 3 hours. A number of radioactive sources were used: ^{109}Cd, ^{57}Co and ^{99m}Tc (see table 2).

Table 2. Radioactive sources used in the experiment, their activity and principal photon energy.

Source	Activity (MBq)	Principal Energy (keV)
^{109}Cd	305	22
^{57}Co	2	122
^{99m}Tc	229	140

2.3.1 Intrinsic spatial resolution

In medical imaging, spatial resolution is one of the most important factors when considering a new device, as it is the accuracy at which the detector is able to distinguish a discrete source.

To measure the intrinsic spatial resolution, a 5 mm thick lead block with a slit of 2 mm width and 20 mm length was placed on top of the detector case and a ^{109}Cd source (7.92 mm in diameter) [10] was placed at a distance of 107 mm above the surface of the lead block in order to produce a uniform flux of X-rays onto the surface to approximate parallel incident photons. Ten images were then taken, each with a total of 999 frames (with each frame having an acquisition time of 100 ms), these were combined and fitted together using ImageJ software [11]. A typical image is shown in figure 3A.

2015 JINST 10 P06012

A line profile was then found by placing a line segment horizontally across the image. The resulting values were analysed using Origin software [12] to find the Edge Response Function (ERF) figure 3B. The derivative of the ERF was taken to produce the Line Spread Function (LSF) figure 3C and the modulus of the LSF was taken to produce figure 3D. The Full Width at Half Maximum (FWHM) and the Full Width at Tenth Maximum (FWTM) were then calculated for each of the LSF peaks, and the average value of the two measurements is shown in table 3. Table 3 also shows an estimation of errors in the FWHM of both peaks.

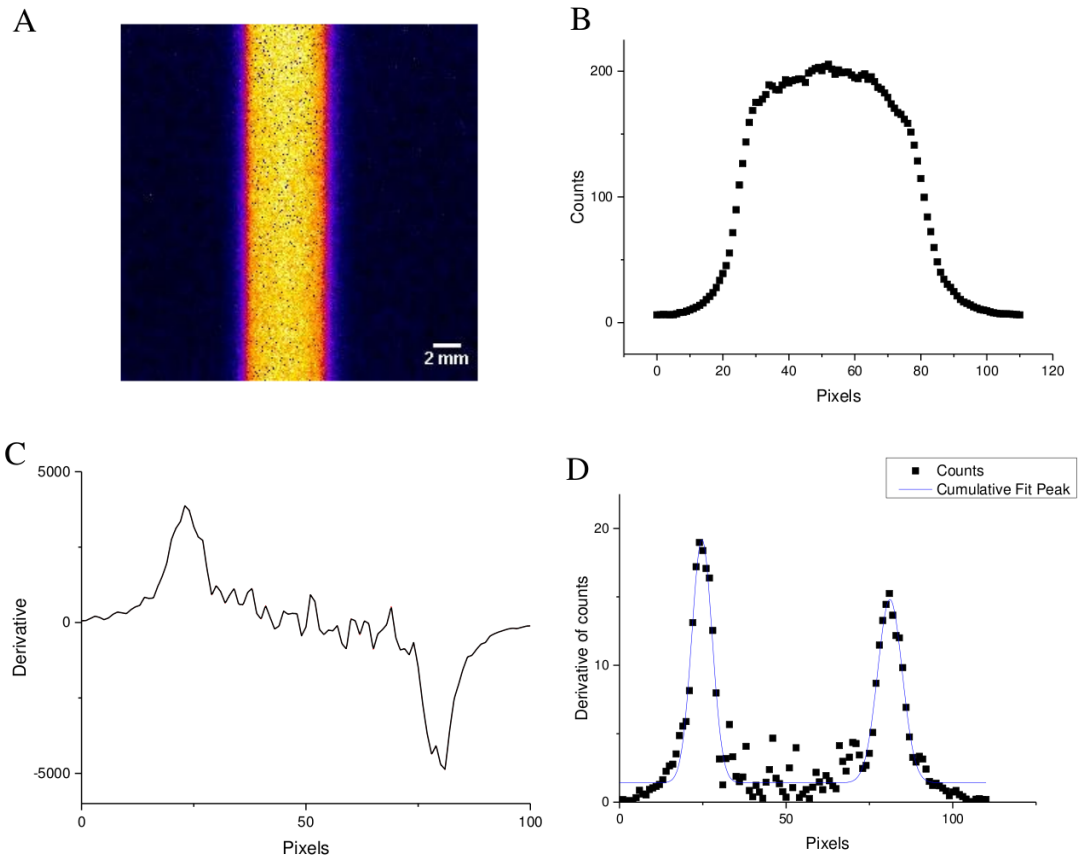

Figure 3. Graphs showing the intrinsic resolution measurement process for the ^{109}Cd source. A) Final summed image of ^{109}Cd at 107 mm distance from the 2 mm width slit. Each sum acquired with a total of 999 frames each frame having an acquisition time of 100 ms. B) ERF for ^{109}Cd source. C) LSF (derivative of ERF). D) Modulus of LSF with fitted Gaussians.

Table 3. Intrinsic spatial resolution result for ^{109}Cd source.

Peak	FWHM (mm)	Error (mm)	FWTM(mm)	Error (mm)
1	0.497	0.024	0.720	0.031
2	0.414	0.017	0.872	0.046
Average	0.456	0.029	0.796	0.038

2015 JINST 10 P06012

2.3.2 System spatial resolution

A more clinically relevant experiment was performed to investigate the spatial resolution of the XRI-UNO. This was achieved by imaging the source with a collimator and suitable scattering media in place. A pinhole collimator was used for imaging as it increases the field of view. Mejia et al. [13] state that by reducing the pinhole's diameter, the spatial resolution is improved. The collimator was a 0.5 mm diameter tungsten pinhole collimator, which measured 6 mm thick and 45 mm in diameter with an acceptance angle of 60̊ [14]. The collimator was placed on top of the detector and masking tape was used to keep it correctly positioned (making sure to only mask the areas around the pinhole). A layer of PMMA poly methyl methacrylate (Perspex) with 9.5 mm thickness was then placed on top of the collimator, with the ^{109}Cd source also positioned on the Perspex and taped down. A 999 frame images was taken having a ∼10 s acquisition time. This process was repeated with more layers of Perspex (increasing up to 47.5 mm in 5 steps of 9.5 mm); increasing the source to detector distance. The experimental setup is illustrated in figure 4, where the pinhole collimator to detector distance is fixed t= 10 mm. the distance between the pinhole collimator to the source being imaged is varied depending on the experiment and this distance determines the demagnification on the detector. Five images of the ^{109}Cd radioisotope source were obtained with different Perspex thicknesses. Figure 5 shows examples of these images. In figure 5A the ^{109}Cd source is 17 mm away from the collimator with 9.5 mm Perspex. And in figure 5B the ^{109}Cd source is 57 mm away from the collimator with 47.5 mm Perspex. All images were processed using ImageJ in order to obtain their line profiles, which were then used to find the spatial resolution. Figure 6 shows the relationship of spatial resolution, both FWHM and FWTM as a function of increasing Perspex thicknesses.

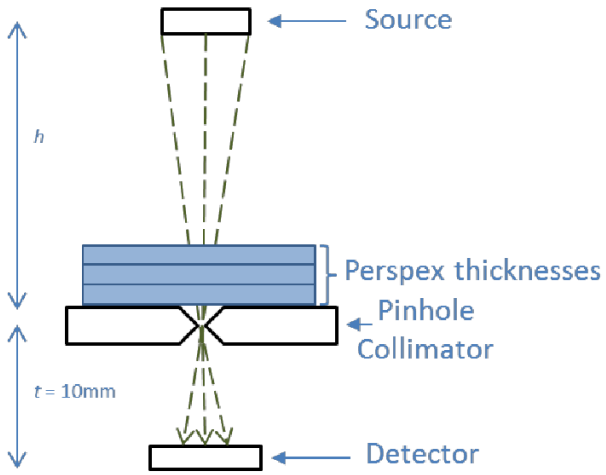

Figure 4. Schematic of the demagnification effect of the pinhole collimator on the detector.

The magnification factor was calculated [15] for each source distance and then used to calculate the actual FWHM and FWTM values. A linear fit was found (Adj. $R^2 = 0.950$) for the FWHM data and (Adj. $R^2 = 0.892$) for the FWTM data. Error bars represent the accuracy of the Gaussian distribution fitting.

2015 JINST 10 P06012

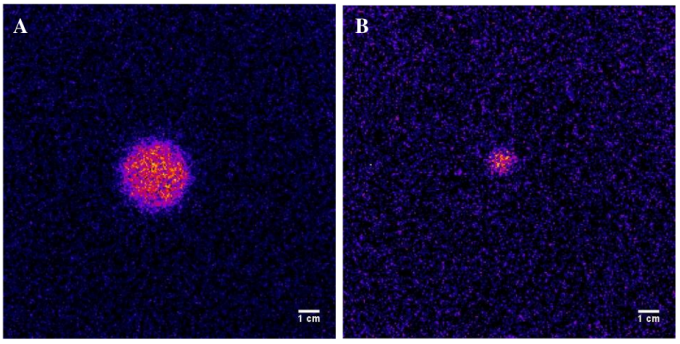

Figure 5. Examples of the ^{109}Cd images taken for system spatial resolution measurements, images acquired with 999 frames. Each frame has an acquisition time of 100 ms. A) ^{109}Cd source at 17 mm away from the collimator with 9.5 mm Perspex thickness. B) ^{109}Cd source at 57 mm away from the collimator with 47.5 mm Perspex thickness.

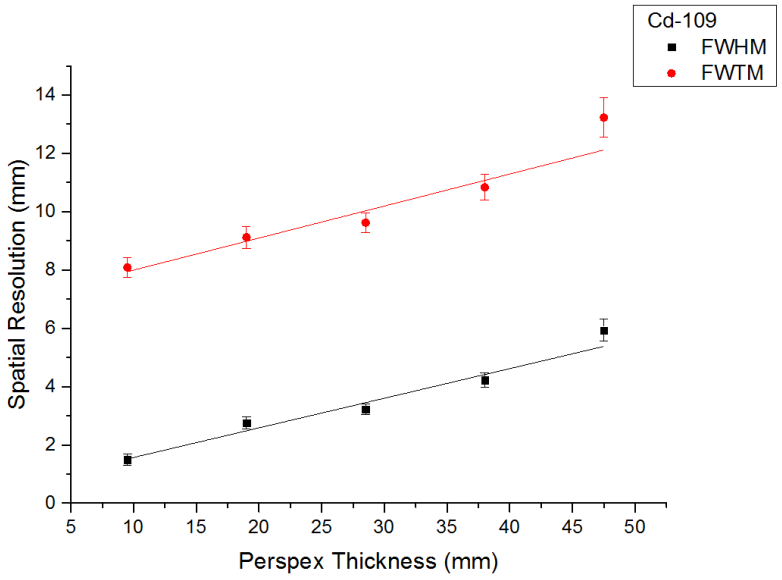

Figure 6. Spatial resolution vs Perspex thickness. FWHM (black squares) and FWTM (red dots) calculated for a ^{109}Cd source with a 0.5 mm diameter pinhole collimator. Each point was calculated from an average of 999 frames, each frame having an acquisition time of 100 ms.

Commonly, the resolution of a LFOV cameras is given as a single value, measured at the collimator face. The FWHM of the XRI-UNO detector can be calculated for any known distance using slope-intercept formula from the line fit, equation (2.2):

$$\mathrm{FWHM} = 0.554 + 0.1057d \tag{2.2}$$

where d is the distance from the detector to the source. When $d = 10$ mm, the distance between the detector and the collimator face, the source is said to be at the non-magnifying position. Thus, the system spatial resolution FWHM value at the non-magnifying position was found to be 1.61 mm.

2015 JINST 10 P06012

2.3.3 Intrinsic spatial uniformity

Several quantitative measurements can be made of the spatial uniformity of a detector; integral uniformity and differential uniformity. For this investigation the standard measurements suggested in the IPEM report 86 [16] were used. The integral uniformity (IU) (i.e. across the entire detector) was calculated using:

$$\mathrm{IU} = \frac{C_{\max} - C_{\min}}{C_{\max} + C_{\min}} \times 100 \tag{2.3}$$

where, $C_{\max}$ and $C_{\min}$ are the maximum and minimum counts detected per pixel by the detector. Equation (2.3) gives the overall uniformity of the detector, to look at the local variations the differential uniformity (DU) can be calculated using equation (2.3) for a small localised group of pixels. IPEM suggest calculating the DU 10 times for each pixel by using the closest five pixels in a row and a column across an entire image, and then calculating the mean of these values.

The image used to measure the spatial uniformity was produced by taking a flood image of a ^{57}Co source (6 mm in diameter) [10] placed at a distance of 107 mm away from the detector, a distance at which it would produce a uniform illumination on to the detector.

Figure 7 shows a typical image produced. It should be noted that in the right upper corner there is an area of non-uniformity.

The IU for any detector is 100% if there is a minimum count value of 0, which was the case for these images. Therefore, IPEM report 86 [16] suggests a more useful measure is the coefficient of variation (COV) which is the standard deviation of counts per pixel divided by the mean counts. The COV of the XRI-UNO detector is 38%. The DU for this detector was found to be 5.174%.

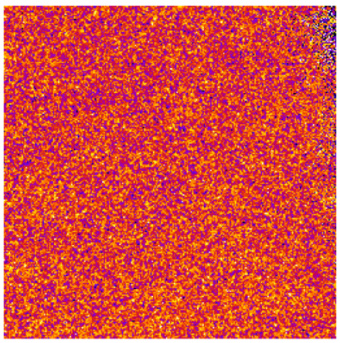

Figure 7. A raw flood image of a ^{57}Co source placed at 107 mm away from the detector to measure the spatial uniformity.

2.3.4 Intrinsic sensitivity

Intrinsic sensitivity is a quantitative measure of the detector's ability to measure incident photon counts. To measure the intrinsic sensitivity, a ^{109}Cd source was placed at a fixed distance of 357 mm away from the surface of the detector with increasing layers of Perspex (ranging from 0–65 mm) on top of the detector. The sensitivity was calculated by dividing the total recorded counts by the incident counts on the detector. The incident counts were calculated using the solid angle, the

2015 JINST 10 P06012

known activity of the source, the distance to the detector and the detector size; equation (2.4):

$$\Omega = 4\tan^{-1}\frac{ab}{2h\sqrt{4h^2+a^2+b^2}} \tag{2.4}$$

Where, (Ω) is the solid angle, (h) source to detector distance and (ab) is the dimension of the detector (i.e. height and width). Each of the images were analysed and the sensitivity calculated, figure 8. An exponential curve was fitted (Adj. $R^2 = 0.988$) to the data shown in Figure 8. The experimental sensitivity was found to be 99% for the ^{109}Cd source with (22 keV energy), this is in close agreement with the theoretical sensitivity of 99% calculated with the known detector parameters; thickness, mass attenuation and density. The sensitivity for the ^{99m}Tc source (140 keV) was calculated at 31.3%.

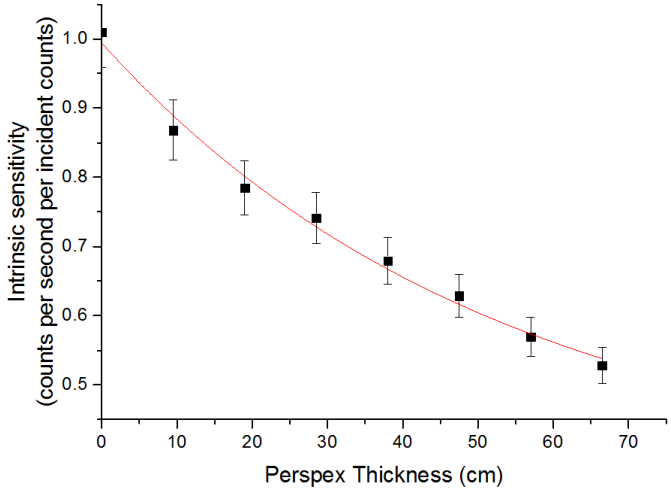

Figure 8. A ^{109}Cd source placed at 357 mm away from the detector with increasing layers of Perspex added in between to show the relationship between the intrinsic sensitivity of the detector and the Perspex thickness.

A comparison of theoretical and experimental values is shown in figure 9.

2.3.5 Count rate capability

To measure the count rate capability of the detector — its ability to linearly measure counts — a container of ^{99m}Tc source (10MBq) was placed directly on top of the detector to allow for maximum saturation. In addition to ^{99m}Tc being the main radionuclide used in nuclear medicine this source was chosen due to its short half-life (6 hours). Images of 999 frames were taken over a period of 3 days. Incident counts were plotted against measured counts to produce a count rate capability curve (see figure 10). A linear fit is calculated for the linear proportional section of the curve (Adj. $R^2 = 0.999$) which indicates that the XRI-UNO detector behaves linearly until at least 1680 counts per second (cps) incident on the detector.

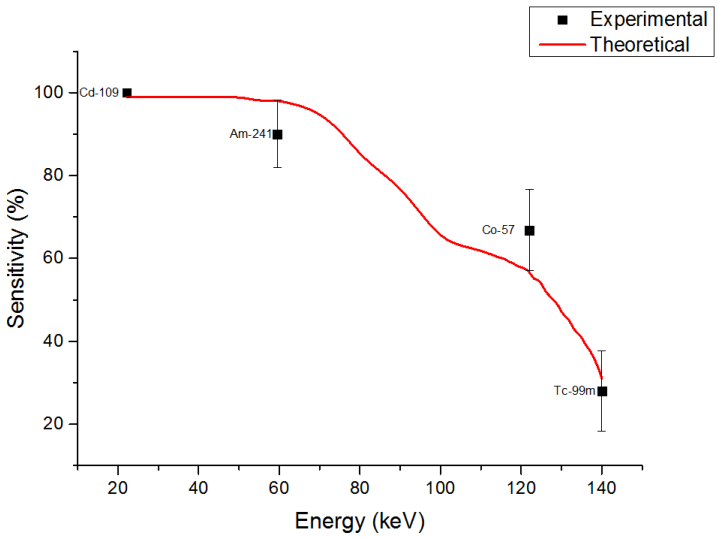

Figure 9. Sensitivity measurements for ^{109}Cd (22 keV), ^{241}Am (59.5 keV), ^{57}Co (122 keV) and ^{99m}Tc (140 keV).

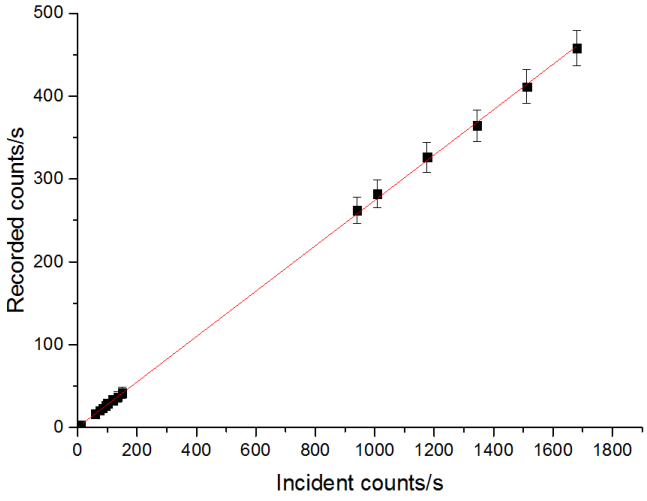

Figure 10. Recorded count rate capability for XRI-UNO detector by using ^{99m}Tc source placed directly on top of the un-collimated detector. Images were taken over the course of 3 days, 999 frame images were used with each frame having an acquisition time of 100 ms.

2.3.6 Contrast to noise ratio

Image noise is a very important parameter in medical imaging. There are two types of image noise; random and structured noise. Random noise is the main cause of concern in nuclear medicine, and can be present everywhere in the image. Random noise can reduce the detectability of the system especially if the source being imaged has low contrast. The critical factor for detectability

2015 JINST 10 P06012

is the contrast to noise ratio (CNR) of the source in the image. Detectability of the source not only depends on the contrast of the source, but also on the size of the source imaged and on the background noise [17]. The CNR can be calculated using the following equations [18]:

$$CNR = \frac{C}{COV} \tag{2.5}$$

$$C = \frac{(N_l - N_{bg})}{N_{bg}} \tag{2.6}$$

$$COV = \frac{\sigma_{bg}}{N_{bg}} \tag{2.7}$$

Where C is the contrast that is measured with consideration of a background region. N_l is the average number of counts per pixel measured in the region of interest (ROI). N_{bg} is the average number of counts of the background, COV is the coefficient of variation, σ_{bg} is the standard deviation of the background. To measure the CNR of the detector, a ^{109}Cd source was placed at fixed distance 100 mm from the collimator while the collimator to detector distance was varied from 10 mm to 40 mm. The collimator used was a 0.5 mm diameter pinhole. Images were acquired with 999 frames and each frame had an acquisition time of 100 ms. A 'ROI' region was defined based on visual inspection of the image of the source and a 'noise' region of identical size was also chosen. The CNR was calculated for each image and the results are shown in figure 11.

An exponential fit was calculated (Adj. $R^2 = 0.995$) for the CNR data and also is plotted on figure 11.

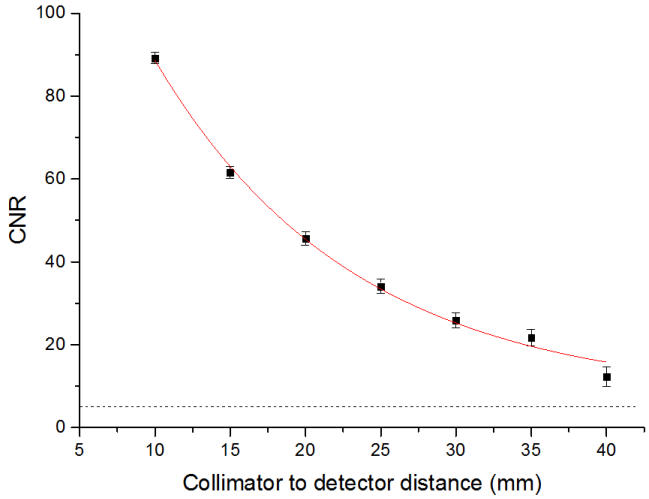

Figure 11. Contrast to noise ratio (CNR) of a ^{109}Cd source placed at 100 mm away from the 0.5 mm pinhole collimator. Distance from collimator to detector was varied from 10 mm to 40 mm.

3 Results and discussion

Table 4 contains the measured performance characteristics for the intrinsic spatial resolution, intrinsic spatial uniformity, intrinsic sensitivity and count rate capability of the XRI-UNO detector. System spatial resolution results are also presented, using a 0.5 mm pinhole collimator.

2015 JINST 10 P06012

Table 4. Performance characteristics for XRI-UNO detector. Extrinsic measurements were taken with a 0.5 mm diameter pinhole collimator.

Detector		CdTe
Field of view (mm)		14.08×14.08
Intrinsic spatial resolution	FWHM (mm)	0.456
	FWTM (mm)	0.796
System spatial resolution	FWHM (mm)	1.61
	FWTM (mm)	8.00
Intrinsic spatial uniformity	Integral uniformity (%)	100
	Mean differential uniformity (%)	5.17
	Co-efficient of variation (%)	38
Intrinsic Sensitivity	(%) at 22 keV	99
Count rate capability	Maximum incident counts/s	1680

The measured intrinsic spatial resolution of the XRI-UNO detector shows that the XRI-UNO operates with a small spatial resolution. This is expected as the XRI-UNO is a direct photon counting device. However a detector's intrinsic resolution is usually much smaller than that of the entire system and the system spatial resolution is a more clinically relevant value. In this investigation a 0.5 mm diameter pinhole collimator was used to assess the spatial resolution of the XRI-UNO detector. As stated previously by Mejia et al. [13] the pinhole's diameter can be reduced to improve the spatial resolution but this would be at the cost of the sensitivity of the detector. Also, single pinhole collimators are better than multi-hole collimators in improving the spatial resolution because of the associated intrinsic magnification factor. The magnification factor is the ratio between the collimator to source distance and the collimator to detector distance. So with this in mind the system spatial resolution of the detector was determined and was found to have a value of 1.61 mm at the non-magnifying point using a 0.5 mm diameter pinhole collimator.

From the measurements of spatial uniformity, it is interesting to note that in the upper right corner figure 7, there is an area of non-uniformity. The exact reason is currently unknown but may be the result of radiation degradation [19] , minor mechanical or electrical damage to the detector. As the integral uniformity for the XRI-UNO may provide inappropriate values, the COV was measured instead. The COV for the XRI-UNO is 38%. The mean differential uniformity of the XRI-UNO was found to be 5.17%.

After investigating the intrinsic sensitivity, it was found that using the ^{109}Cd source with an energy of 22 keV, the sensitivity was approximately 99%. This is remarkably close to the 99% theoretical efficiency calculated for the ^{109}Cd source at 22 keV energy.

The detector has a linear count rate up to at least 1680counts per second (cps) incident.

For contrast to noise ratio there was a declining trend as the collimator to detector distance increases, which is thought by Strauss [20] to be mainly due to the decrease in contrast caused by increasing the distance, as fewer photons are detected by the detector. In addition, according to Dickerscheid [18] a loss in resolution will reduce the CNR due to scatter and attenuation. The

2015 JINST 10 P06012

Rose criterion states that "if the CNR of a hotspot becomes smaller than 3 to 5, it becomes very difficult to observe the hotspot" [21]. In the XRI-UNO detector the worst ratio detected at furthest distance measured (i.e. 40 mm collimator to detector distance) is 12. This value suggests that the detector has the ability to detect the source used as it was above the threshold value.

4 Conclusion

The performance of the XRI-UNO has been investigated indicating that a further characterisation of the full clinical performance, including energy resolution, should be carried out. The results presented in this paper show that the XRI-UNO has promising performance for use with lower energies less than 30 keV, but due to relatively thin CdTe layer would not be suitable for imaging with higher energy radionuclides such as ^{99m}Tc, which is most commonly used in clinical nuclear imaging.

Acknowledgments

The authors would especially like to thank the X-Ray Imatek Company for the detector loan. Glyn White, Advatech for his advice and support. Also, the authors would like to thank the staff at the Leicester Royal Infirmary for their support, in particular David Monk and Helen Hill. We also acknowledge the technical support from William McKnight, Space Research Centre, University of Leicester. This work was supported by studentships from King Saud University, Riyadh, Saudi Arabia, King Khalid University, Abha, Saudi Arabia, Ministry of Education, Saudi Arabia, Saudi Cultural Bureau, London, United Kingdom, Science and Technologies Facilities Council studentship and the Summer Undergraduate Research Experience (SURE) program at the University of Leicester.

References

[1] N.M. Hung, J. Joung, K. Lee and Y. Kim, *Development of correction schemes for a small field of view gamma camera*, *Biomed. Engin. Lett.* **2** (2013) 215.

[2] Y. Eisen, A. Shor and I. Mardor, *CdTe and CdZnTe x-ray and gamma-ray detectors for imaging systems*, *IEEE Trans. Nucl. Sci.* **51** (2004) 1191.

[3] M. Tsuchimochi et al., *A prototype small CdTe gamma camera for radioguided surgery and other imaging applications*, *Eur. J. Nucl. Med. Mol. Imaging* **30** (2003) 1605.

[4] S. Yin et al., *Direct conversion CdZnTe and CdTe detectors for digital mammography*, *IEEE Trans. Nucl. Sci.* **49** (2002) 176.

[5] P. Russo et al., *Evaluation of a CdTe semiconductor based compact gamma camera for sentinel lymph node imaging*, *Med. Phys.* **38** (2011) 1547.

[6] X.-R. Imatek, *XRI-UNO/CdTe Manual*, Eureka, Barcelona Spain (2012).

[7] G.F. Knoll, *Radiation Detection and Measurement*, third edition, Wiley, New York U.S.A. (2000), pg. 802.

[8] R. Redus, *Efficiency of Amptek XR-100T-CdTe and CZT Detectors Application Note ANCXT-1 Rev 2*, in *CdTe/CZT Application Note*, Amptek Inc., Bedford U.S.A. (2002).

2015 JINST 10 P06012

[9] J.H. Hubbell and S.M. Seltzer, *X-Ray mass attenuation coefficients*, NIST, Physical Measurement Laboratory 2009. Available from: http://physics.nist.gov/PhysRefData/XrayMassCoef/ComTab/telluride.html.

[10] Eckert&Ziegler, *Industrial radiation sources*, E.Z.I. Products, Valencia U.S.A. (2008).

[11] M.D. Abramoff, P.J. Magalhaes and S.J. Ram, *Image Processing with ImageJ*, *Biophotonics International* **11** (2004) 36.

[12] OriginLabCorporation, *OriginLab*. Available from: http://www.originlab.com/doc/.

[13] J. Mejia et al., *A clinical gamma camera-based pinhole collimated system for high resolution small animal SPECT imaging*, *Brazilian J. Med. Biol. Res.* **43** (2010) 1160.

[14] Ultimate Metals, 46 Larkshall Road, E4 7HZ Chingford London, U.K.

[15] S.L. Bugby, J.E. Lees, B.S. Bhatia and A.C. Perkins, *Characterisation of a high resolution small field of view portable gamma camera*, *Phys. Med.* **30** (2014) 331.

[16] IPEM, *Quality control of gamma camera system*, Institute of Physics and Engineering in Medicine, York U.K. (2003).

[17] S.R. Cherry, J.A. Sorenson and M.E. Phelps, *Image Quality in Nuclear Medicine*, in *Physics in Nuclear Medicine*, Elsevier/Saunders, Amsterdam The Netherlands (2012), pg. 233.

[18] D. Dickerscheid, J. Lavalaye, L. Romijn and J. Habraken, *CNR analysis and optimisation of breast specific gamma imaging acquisition protocol*, *EJNMMI Research* **3** (2013) 1.

[19] A. Cavallini et al., *Radiation effects on II–VI compound-based detectors*, *Nucl. Instrum. Meth.* **476** (2002) 770.

[20] L.J. Strauss and W.I. Rae, *Image quality dependence on image processing software in computed radiography*, *South African J. Radiol.* **16** (2012) 44.

[21] A. Rose, *The Visual Process*, in *Vision Human and Electronic*, Plenum Press, New York U.S.A. (1974).

2015 JINST 10 P06012